Polarimetric Signatures of Midlatitude Warm-Rain Precipitation Events

N. CARR

School of Meteorology, University of Oklahoma, and Advanced Radar Research Center, National Weather Center, Norman, Oklahoma, and The Climate Corporation, Seattle, Washington, and NOAA/National Weather Service, Salt Lake City, Utah

P. E. KIRSTETTER

Advanced Radar Research Center, National Weather Center, and NOAA/National Severe Storms Laboratory, Norman, Oklahoma

J. J. GOURLEY

NOAA/National Severe Storms Laboratory, Norman, Oklahoma

Y. HONG

Advanced Radar Research Center, National Weather Center, and School of Civil Engineering and Environmental Sciences, University of Oklahoma, Norman, Oklahoma

(Manuscript received 19 April 2016, in final form 20 October 2016)

ABSTRACT

Precipitation events in which rainfall is generated primarily below the freezing level via warm-rain processes have traditionally presented a significant challenge for radar and satellite quantitative precipitation estimation (QPE) algorithms. It is possible to improve QPE in warm-rain events if they are correctly identified/classified as warm rain prior to precipitation estimation. Additionally, it is anticipated that classification schemes incorporating polarimetric radar data will be able to leverage precipitation microphysical information to better identify warm-rain precipitation events. This study lays the groundwork for the development of a polarimetric warm-rain classification algorithm by documenting the typical three-dimensional polarimetric characteristics associated with midlatitude warm-rain precipitation events. These characteristics are then compared with those observed in non-warm-rain events. Nearly all warm-rain precipitation events were characterized by lower median values of Z, Z_{DR}, and K_{DP} relative to the non-warm-rain convective cases. Furthermore, droplet coalescence was determined to be the dominant microphysical process in the majority of warm-rain events, while in non-warm-rain stratiform events, evaporation and breakup appeared to be the dominant (warm) microphysical processes. Most warm-rain events were also associated with sharp decreases in reflectivity, with height above the freezing level coincident with low echo-top heights and freezing-level Z_{DR} values near 0, indicating limited ice- and mixed-phase precipitation growth processes. These results support the feasibility of a future polarimetric warm-rain identification algorithm.

1. Introduction

Flooding caused by excessive precipitation poses a significant threat to lives and property and consistently ranks as one of the most destructive natural disasters (Adhikari et al. 2010). A particular type of precipitation event in which precipitation growth occurs primarily below the freezing level through the collision–coalescence process, often termed warm rain, can be especially dangerous from a flooding perspective (Baeck and Smith 1998; Nicosia et al. 1999). The dangerous flooding potential associated with warm-rain events is due to both the relative efficiency of warm precipitation growth processes and the tendency for radars and passive spaceborne sensors to produce poor and unreliable precipitation estimates (Chen et al. 2011; Grams et al. 2014). These unreliable precipitation estimates severely inhibit the ability of forecasters and emergency managers

Corresponding author e-mail: Nick Carr, n.carr2@ou.edu

DOI: 10.1175/JAMC-D-16-0164.1

to provide timely warnings of potential flooding events (Vitale and Ryan 2013; Grams et al. 2014).

The tendency for radars to underestimate rainfall accumulations in warm-rain precipitation events is a consequence of both the drop size distributions (DSD) and the vertical structure of precipitation associated with these events. Specifically, warm-rain events are characterized by DSDs consisting of relatively high concentrations of small drops (Squires 1956; Ulbrich and Atlas 2008) and median droplet size increasing (below the freezing level) toward the surface (Xu et al. 2008). These microphysical characteristics are distinct from those typically observed in midlatitude convective and stratiform precipitation events, in which precipitation growth is dominated by ice- and mixed-phase processes (i.e., processes occurring above the freezing/melting level). It has been demonstrated that radar quantitative precipitation estimation (QPE) can be improved in warm-rain events if they are accurately identified (as warm rain) prior to precipitation estimation (Xu et al. 2008; Grams et al. 2014). Current state-of-the-science radar precipitation classification algorithms utilize a combination of single-polarization radar data and environmental data to identify warm-rain precipitation (Grams et al. 2014). Although these algorithms are an improvement over previous classification methods, the limited precipitation microphysical information available in single-polarization radar data limits their effectiveness. Additional classification methods utilizing satellite and lighting flash rate data are promising but are currently limited by data availability (Zipser and Lutz 1994; Petersen et al. 1999).

Polarimetric radar data can provide detailed information regarding the microphysical properties of precipitation, such as hydrometeor phase, size, shape, and orientation (Zrnic and Ryzhkov 1999; Ryzhkov et al. 2005). Additionally, various microphysical processes have been observed to result in distinct three-dimensional polarimetric signatures or "fingerprints" (Kumjian et al. 2012; Kumjian and Prat 2014). By analyzing these signatures, it is often possible to discern the dominant precipitation microphysical processes at work in a particular precipitation event. The polarimetric signatures and characteristics associated with warm-rain precipitation and warm-rain processes have been observed in limited observational studies (Lang et al. 2010; Rutledge et al. 2013; Kumjian and Prat 2014) and numerical simulations (Kumjian and Prat 2014). However, prior to the 2013 dual-polarization (dual pol) upgrade to the U.S.'s Next Generation Weather Radar (NEXRAD) network, a comprehensive evaluation of the polarimetric characteristics associated with warm-rain events has been infeasible.

This study capitalizes on the 2013 dual-pol upgrade to the NEXRAD radar network to thoroughly document the polarimetric characteristics associated with warm-rain precipitation events occurring during the 2014 warm season (April–September inclusive) over the eastern-central conterminous United States (CONUS). First, potential warm-rain events are identified using a conservative case selection procedure, which incorporates radar, rain gauges, and environmental data. Following this case selection procedure, the three-dimensional profiles of the polarimetric radar variables—reflectivity factor at horizontal polarization Z_H, differential reflectivity Z_{DR}, cross-correlation coefficient ρ_{hv}, and specific differential phase K_{DP}—are analyzed for the selected cases. To assist in the analysis, the median polarimetric characteristics associated with each event are mapped onto two special parameter spaces, developed to highlight precipitation microphysical processes and properties. Finally, the polarimetric characteristics of the warm-rain events are compared with the polarimetric characteristics of selected non-warm-rain events in order to inform the development of future polarimetric warm-rain classification schemes.

The polarimetric characteristics observed and documented in this study will help lay the groundwork for the development of a polarimetric warm-rain classification algorithm. It is anticipated that this microphysically based classification algorithm could lead to significant improvements in radar QPE. Additionally, this study may provide an improved understanding of warm precipitation microphysics, which would be useful for more general meteorological applications, including microphysics parameterizations in numerical weather prediction (NWP) models and satellite QPE.

The study is organized as follows: Details regarding data sources and the case selection procedure are presented in section 2. Section 3 details the three-dimensional polarimetric characteristics associated with the selected warm-rain precipitation events and then compares these characteristics with those observed in non-warm-rain events. Concluding remarks and suggestions for future research are provided in section 4.

2. Data sources, case selection procedure, and description of parameter spaces

a. Radar data

All radar data utilized in this study were obtained from the National Climatic Data Center's (NCDC) archive of NEXRAD Level II radar data. Along with the base Level II parameters of Z, Z_{DR}, and ρ_{hv}, the following derived parameters were utilized in this study:

(i) Specific differential phase (K_{DP}) was obtained from the radial profile of Φ_{DP} by applying a finite-differencing

scheme on a smooth spline of Φ_{DP}. The quantity K_{DP} was only calculated on radials with 20 consecutive range gates (~5 km in the radial direction) meeting minimum Z (15 dBZ) and ρ_{hv} (0.92) thresholds. These thresholds were selected to limit noise in the Φ_{DP} field because of low radar signal strength and/or nonuniform beamfilling.

(ii) Echo- and storm-top heights were obtained by mapping the volumetric radar data onto a 1-km^2 Cartesian grid and then determining the maximum height at each grid point where reflectivity values exceeded 18 (echo top) and 30 (storm top) dBZ.

(iii) Slopes of the vertical profiles of the polarimetric variables were obtained via ordinary least squares (OLS) linear regression between the polarimetric variables and beam center height (assuming standard refraction).

(iv) Additional parameters, such as the values of the polarimetric variables relative to the freezing level or melting-layer bottom, were obtained by merging the polarimetric data with the ancillary environmental data detailed in section 2b.

The bulk of the analysis utilized the radar data in its native polar (250 m range–1° azimuth) coordinate system. However, the data were gridded into 2D 1-km^2 Cartesian grid cells for echo/storm-top calculation, and the data were converted into a 3D 1-km Cartesian grid when calculating the difference quantities associated with the Kumjian–Ryzhkov parameter space (described in section 2c).

b. MRMS products

The Multi-Radar Multi-Sensor (MRMS) system is a set of experimental radar products including high-resolution (0.01°, 2 min) instantaneous rainfall rate mosaics available over the CONUS (Zhang et al. 2016). MRMS integrates information from all ground-based radars comprising the WSR-88D and Canadian radar networks, mosaics reflectivity data onto a common 3D grid, and estimates surface precipitation type and amount (Zhang et al. 2005; Lakshmanan et al. 2007; Vasiloff et al. 2007). Additionally, MRMS incorporates ancillary environmental data and rain gauge information in its QPE algorithms.

The following MRMS parameters were utilized in this study:

(i) The radar with gauge bias correction (RWGBC) hourly accumulation product is obtained by modifying the radar-only hourly accumulation estimation at each MRMS grid cell with a bias correction obtained by considering the difference between radar and Hydrometeorological Automated Data System (HADS) gauge hourly accumulation estimates. Specifically, the bias at each MRMS grid cell is determined by interpolating the gauge–radar additive bias calculated at gauge sites using an inverse-distance weighted interpolation scheme. Finally, the RWGBC accumulation value at each grid point is obtained by adding or subtracting the interpolated bias to/from the MRMS radar-only accumulation estimate at that grid cell.

(ii) The hourly radar–gauge ratio (RGR) is the ratio of the radar and gauge hourly accumulation values at gauge locations. RGR values <1 indicate radar underestimation relative to gauges, while values >1 indicate radar overestimation.

(iii) The surface precipitation type (SPT) is obtained at each grid cell via an algorithm that incorporates radar and environmental data to classify the dominant precipitation type (i.e., convective, stratiform, and tropical) in each MRMS grid cell (Zhang et al. 2011; Qi et al. 2013).

(iv) MRMS melting-layer height parameters were also included in the analysis. MRMS obtains the freezing-level height directly from the Rapid Refresh (RAP) model and defines the approximate bounds of the melting layer by synthesizing the RAP freezing-level height with the vertical profile of reflectivity (VPR). While the MRMS melting-layer heights are generally accurate, in this study, the MRMS melting-layer heights were occasionally corrected using the polarimetric melting-layer detection algorithm detailed in Giangrande et al. (2008).

c. Microphysical parameter spaces

It has been demonstrated that by mapping polarimetric radar data onto certain parameter spaces, it is possible to obtain greater insight into the dominant precipitation microphysical processes and properties associated with a given precipitation event. Consequently, the following parameter spaces were utilized to aid in the analysis:

(i) A parameter space defined by an x axis of Z and a y axis of Z_{DR} was developed and utilized to examine the microphysical characteristics of precipitation first by Zhang et al. (2006) over Florida and then by Cao et al. (2008) over Oklahoma (this parameter space is referred to as the CZ parameter space after its developers). A benefit of this parameter space is that the reference curves (derived using disdrometer data) can be considered somewhat representative of the typical Z–Z_{DR} relationships in continental (Oklahoma) and subtropical (Florida) locations. The primary microphysical interpretation of this parameter space is that precipitation events in which most

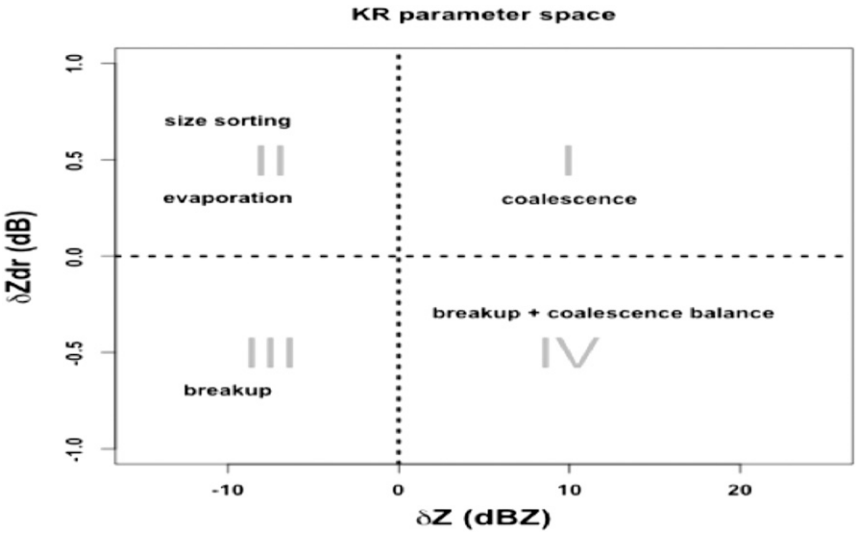

FIG. 1. The locations of warm microphysical processes within the parameter space of δZ and δZ_{DR} (in the liquid layer) developed by Kumjian et al. (2012).

radar pixels lie below the reference curves are characterized by smaller and/or higher concentrations of drops than are typically seen in either the midlatitude continental and/or subtropical locations. This interpretation follows because Z is dependent on both drop size and concentration, whereas Z_{DR} is not directly affected by drop concentration but is highly proportional to drop size.

(ii) Finally, this study also utilizes a parameter space that takes into account the vertical variation of the variables Z and Z_{DR}, developed by Kumjian et al. (2012) and referred to as the Kumjian and Ryzhkov (KR) parameter space (after its principal developers). The x axis of the KR parameter space is defined by the difference in radar reflectivity (δZ; dBZ) between the surface and the bottom of the melting layer (considered to be the top of the liquid layer). The y axis is defined by the difference in differential reflectivity (δZDR) in decibels over the same vertical layer. This parameter space is useful for discerning the dominant warm microphysical process at work in a precipitation event, and Fig. 1 illustrates the locations of warm microphysical processes within the KR parameter space [refer to Kumjian et al. (2012) for a more detailed description]. It is anticipated that in warm-rain events, most points should lie in the first quadrant because coalescence is most likely the dominant warm microphysical process.

d. Case selection procedure

Prior to detailing the warm-rain case selection procedure, it is important to note that the definition of a warm rain in the context of this study is different than the traditional definition of warm rain. Traditionally, warm rain has been defined as rain generated from clouds–cloud systems located entirely below the freezing level. While this (strict) definition rarely applies to midlatitude precipitation events, previous studies have demonstrated that collision–coalescence can in fact be the dominant precipitation growth mechanism in intense midlatitude precipitation events (Petersen et al. 1999; Vitale and Ryan 2013; Gochis et al. 2015). Furthermore, in many of these events, ice-phase hydrometeors were also present, making these warm-rain events microphysically different than the shallow warm-rain systems observed in the tropics (Liu and Zipser 2009). Because the focus of this study is on midlatitude applications, a warm-rain event is herein defined as an event in which precipitation growth occurs primarily below the freezing–melting level via warm-rain processes. It is important to note that, using this expanded definition, some precipitation events containing substantial quantities of mixed- and ice-phase hydrometeors will be correctly considered as warm rain.

While a number of warm-rain identification methods have been developed for applications in the tropics (Liu and Zipser 2009), most of these methods rely on infrared (IR) cloud-top temperatures and are thus not well suited for classifying precipitation events fitting the less strict warm-rain definition provided above. Other identification methods utilizing lighting flash rates (see Petersen et al. 1999) or passive microwave (PMW) satellite data are promising, but these data

sources are currently too spatiotemporally intermittent to generate the sufficiently large warm-rain case dataset needed for a comprehensive study. Consequently, the warm-rain case selection criteria utilized in this study are largely based upon the results of the MRMS SPT classification algorithm, which was developed specifically for midlatitude applications. Concretely, all significant (in size and intensity) precipitation events classified by MRMS as ''tropical'' (the term MRMS uses for warm rain) were initially considered for the polarimetric analysis.

A known issue with the MRMS tropical precipitation identification algorithm (detailed in Grams et al. 2014) is that it tends to overclassify precipitation as tropical (Chen et al. 2013; Zhang et al. 2016). Therefore, to reduce the number of ''false alarms'' included in the warm-rain dataset, the following additional case selection criteria were applied using the MRMS parameters detailed in section 2b:

(i) Because the results of the MRMS SPT classification algorithm dictate the form of the reflectivity–rain rate (Z–R) relationship applied at a given MRMS pixel, a large discrepancy between radar precipitation estimates and gauge estimates potentially indicates errors in the pixel's SPT classification (although additional factors can influence the quality of radar precipitation estimates). The tropical Z–R relation is rather aggressive (i.e., results in a relatively large rainfall rate for a given value of Z). Consequently, when MRMS incorrectly classifies a grid cell as tropical, that cell's precipitation estimate will often be positively biased relative to gauge accumulations (Kirstetter et al. 2015). Consequently, we require that the mean MRMS RGR within the tropically classified precipitation feature is <1.05.

(ii) We also required that the majority of the tropically classified precipitation features be located between 20 and 80 km from a radar site. This requirement was implemented to both improve low-level radar sampling and also limit the effects of beam broadening at far ranges.

(iii) The mean hourly RWGBC accumulation was required to be at least 10 mm. This threshold was implemented to both limit noise in the polarimetric variables and also focus the analysis on significant precipitation events.

After implementing the case selection procedure outlined above, 49 warm-rain events were selected for further analysis from all precipitation classified by MRMS as tropical occurring over the eastern-central (east of 102°W) CONUS from April to September 2014. The locations and months of occurrence of these handpicked warm-rain cases are displayed in Fig. 2. It can be observed from Fig. 2 that the chosen cases demonstrate considerable spatiotemporal diversity, including a landfalling tropical cyclone (Hurricane Arthur) along with more ''typical'' midlatitude precipitation events.[1]

Precipitation events in which precipitation was likely not generated primarily via warm-rain processes were also selected for comparison purposes. These cases were selected from the same spatiotemporal domain as the warm-rain cases, and the basis for classification was once again the MRMS SPT classification. We required that MRMS classify the precipitation as nontropical, convective, or stratiform. The same distance (20–80 km) and minimum hourly accumulation (10 mm) thresholds were also enforced. There were many precipitation events meeting the non-warm-rain selection criteria; however, 42 meteorologically (e.g., squall line, frontal, and widespread stratiform) and geographically representative non-warm-rain cases were subjectively selected for comparison.

Certain warm-rain cases meeting the classification criteria were occasionally further broken down into precipitation features (PFs) primarily on the basis of the low-level reflectivity field and the spatial distribution of the RGR. This step was performed to both limit the impact of microphysical heterogeneity within the precipitation field and remove areas of likely misclassified (by MRMS) precipitation from the analysis. Figure 3 shows an example of a case in which a PF was defined within a larger precipitation field. Figure 3a demonstrates that the majority of the precipitation occurring near the center of the map (located in the central part of the state of Arkansas) was classified by MRMS as tropical for this event. However, from Fig. 3b, it is notable that, although the mean RGR in the tropical precipitation region was <1.05 (meeting our criteria), most of the stratiform precipitation[2] in the western part of the figure was associated with RGRs > 1.05 (meaning radar overestimated relative to the gauge). Consequently, it is likely that this stratiform precipitation was erroneously classified as tropical by MRMS, and therefore, we define the PF shown by the red polygon in Fig. 3c and only perform polarimetric analysis on this portion of the precipitation field.

[1] A future, more detailed study on the three-dimensional polarimetric characteristics of Hurricane Arthur is anticipated.

[2] Note that ''warm stratiform'' per MRMS' classification methodology is not stratiform with enhanced warm-rain processes but rather is conventional stratiform occurring at surface temperatures > 5°C (refer to Fig. 10 in Zhang et al. 2016).

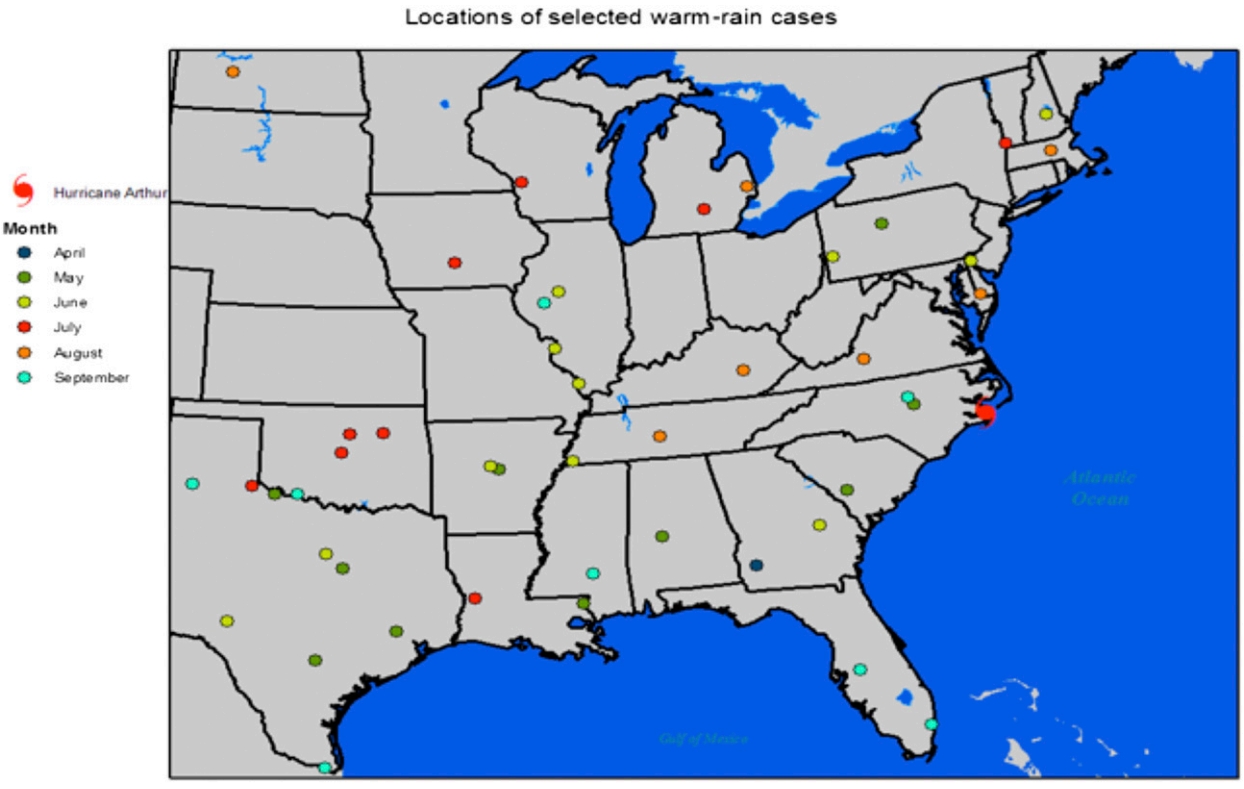

FIG. 2. Locations of the selected warm-rain cases. The circle fill color corresponds to the month of occurrence, and Hurricane Arthur is given a unique symbol.

It must be emphasized that despite the conservative case selection procedure, there is no guarantee that the selected warm-rain cases are warm-rain events, and the converse is also true for the non-warm-rain events. However, the case selection procedure was designed to be intentionally conservative, and it will be hereafter assumed that the selected events are correctly categorized. Ideally, future studies will be able to use the polarimetric characteristics documented in this study to identify warm-rain events more objectively.

3. Analysis and results

a. Liquid-layer polarimetric characteristics

All radar pixels located below the melting-layer bottom are considered as ''liquid'' pixels in the subsequent analysis. Although this definition possibly erroneously classifies some pixels containing partially melted hail and graupel as liquid, the impacts of hail and graupel contamination are limited by imposing hail caps (e.g., gates containing Z values >60 dBZ were not included in the analysis). Additionally, this section of the analysis focuses on warm-rain events, which generally are not associated with environmental conditions conducive to hail formation (Grams et al. 2014). The number of liquid radar pixels (N) analyzed for each case is a function of several factors, including the size of the precipitation feature, the volume coverage pattern (i.e., the scanning strategy) employed by the radar operator, the depth of the liquid layer, the distance between the precipitation feature and the radar site, and the number of pixels meeting the selection criteria detailed in section 2a. Consequently, N for each case varies from 3000 to 100 000 pixels with the median N being 22 320 pixels.

The initial analysis focused on documenting polarimetric characteristics associated with each individual warm-rain event. Following this initial analysis, it was determined that in the vast majority of cases, the precipitation event can be adequately described by its median polarimetric characteristics. This is largely due to the manual precipitation feature selection procedure described in section 2d, in which great care was taken to group radar precipitation features on the basis of homogenous microphysical characteristics. The bulk of the subsequent analysis therefore deals with the median polarimetric characteristics associated with each precipitation event. It is anticipated that future studies may

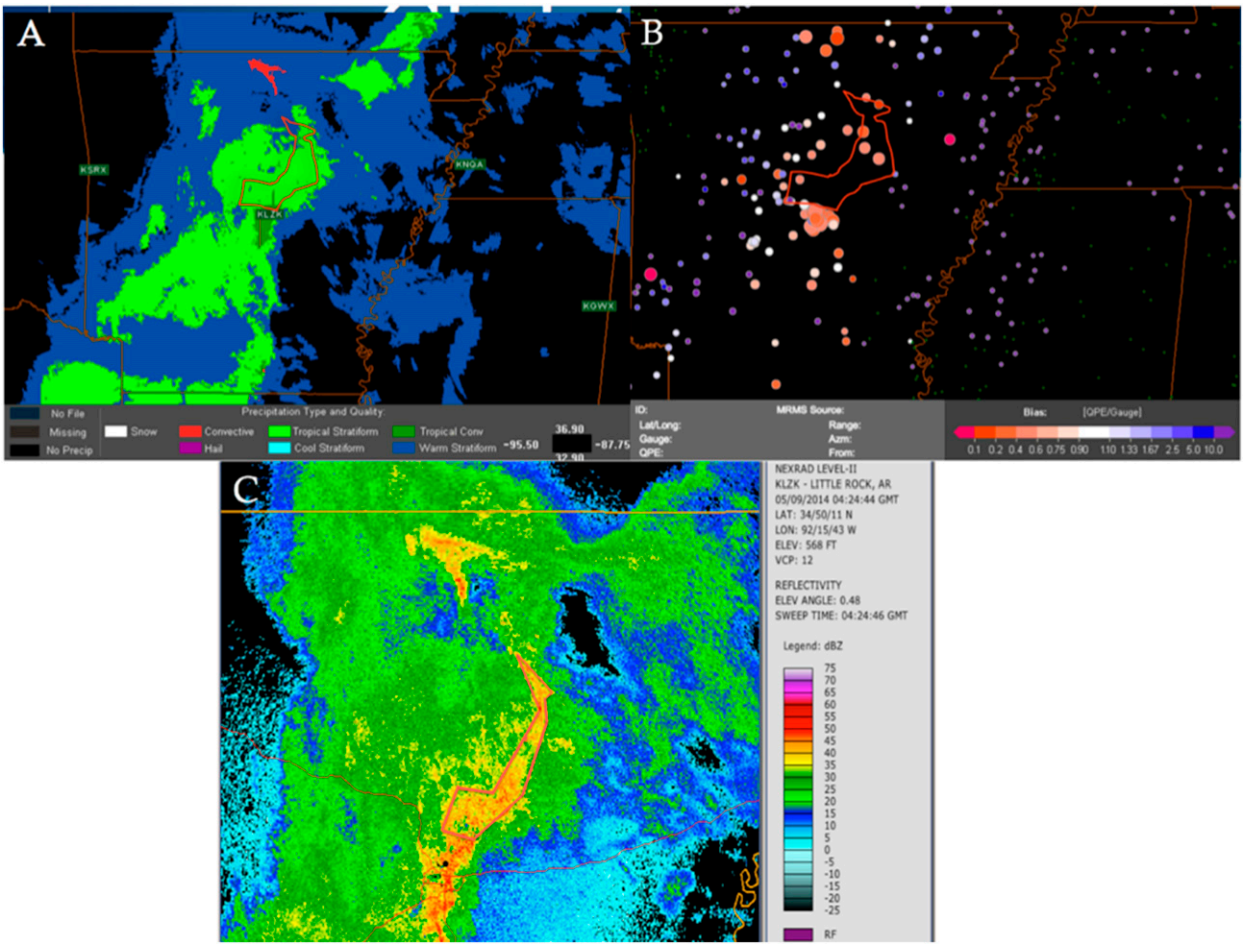

FIG. 3. An example of a situation in which a PF was defined within a broader precipitation field. The red polygon denotes the portion of the PF that was deemed to be correctly classified as tropical and thus included in the analysis. (a) The MRMS SPT classification for a particular volume scan. (b) The hourly RGR, in which ''warm''-colored circles represent gauges where the radar underestimated precipitation. (c) The low-level reflectivity field for the same event.

focus on specific warm-rain precipitation events in greater detail [e.g., as is done in Gochis et al. (2015)].

Figure 4 displays histograms of the median liquid-layer Z, Z_{DR}, and K_{DP} values for the warm-rain cases, and Table 1 provides associated descriptive statistics. It is evident that there is considerable variation between cases in the median polarimetric parameter values, with median Z values ranging from 32 to 45 dBZ, Z_{DR} values ranging from 0.1 to 1.6 dB, and K_{DP} values ranging from 0.0° to 1.2° km^{-1}.

Figure 5 displays the median Z and Z_{DR} values associated with each case relative to the Florida and Oklahoma reference curves. From this figure, it is clear that the majority of the warm-rain cases are characterized by lower Z_{DR} values than would be expected for a given Z value in a continental region, highlighting the likely presence of large concentrations of smaller-than-average drops. Only 6 out of 49 cases have median Z–Z_{DR} values above the Oklahoma–continental curve, and the majority of the cases (29) are also located below the Florida–subtropical curve. Surprisingly, several of the northern cases (occurring at latitudes > 40°N) were located well below the Florida curve, implying that precipitation with tropical microphysical characteristics can be observed well into the midlatitudes.

b. *Vertical variation in polarimetric characteristics*

Figure 6 displays the median vertical polarimetric profiles for each case, along with the average warm-rain profile obtained via a weighted (by number of radar pixels) average of all the cases, and the final columns of Table 1 provide associated descriptive statistics regarding the vertical profiles of the polarimetric variables. From these data, it is evident that, in general, warm-rain events are characterized by negative slopes of Z below the melting level. This result is expected, as all

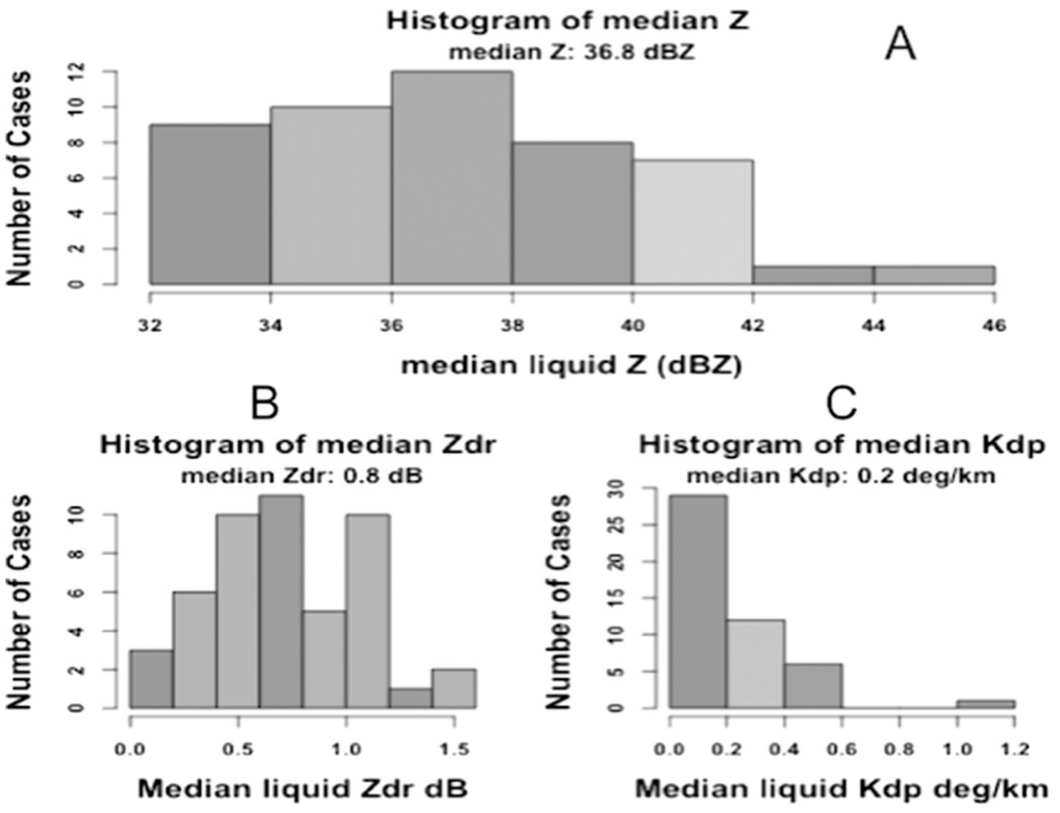

FIG. 4. Histograms of the median polarimetric variables (a) Z, (b) Z_{DR}, and (c) K_{DP} associated with each warm-rain case. The (unweighted) median value for all cases in aggregate is provided above each histogram.

selected cases were classified as tropical by MRMS, and the MRMS tropical classification is highly contingent on the slope of the radar-averaged VPR below the melting level being 0 or negative (Grams et al. 2014). What is surprising is that despite this criterion, 11 of the 49 cases were actually associated with positive VPR slopes below the melting–freezing level, and 7 cases were associated with positive slopes $>1\,\mathrm{dB}Z\,\mathrm{km}^{-1}$, implying significant decreases in reflectivity toward the surface. This result is partially due to the fact that MRMS calculates the slopes of the vertical profiles using a different method (maxima search) than the regression-based technique employed in this study but also occurs because the VPR MRMS uses in its SPT classification is the average VPR of all MRMS pixels between 20 and 80 km of the radar site, while this study calculates VPRs for specific precipitation features. Note that, although we only incorporated radar data fairly close to radars (20–80 km from the radar site) in the analysis, it is possible that some of the observed noise in the vertical profiles shown in Fig. 6 (particularly ρ_{HV} and K_{DP}) results from the blending of radar data obtained at different ranges/tilts

TABLE 1. Descriptive statistics of the polarimetric variables for the selected warm-rain events: median, mean, and 25th and 75th percentiles.

Statistic	Median	Mean	25th	75th	Min	Max
Median liquid Z (dBZ)	36.75	37.06	6	39.12	32	45
Median liquid Z_{DR} (dB)	0.8	0.77	0.5	1.1	0.1	1.6
Median liquid K_{DP} (° km^{-1})	0.2	0.25	0.1	0.3	0.0	1.2
Pixels below the CZ Oklahoma curve (%)	76	71	59	86	25	99
Pixels below the CZ Florida curve (%)	66	61	45	80	16	98
Slope Z liquid phase (dBZ km^{-1})	−0.6	−0.31	−1	0.0	−2.3	2.6
Slope Z_{DR} liquid phase (dB km^{-1})	0.0	−0.06	−0.1	0.0	0.1	−0.2
Slope K_{DP} liquid phase (° km^{-2})	0.0	−0.04	−0.1	0.0	−0.2	0.1
Slope Z ice phase (dBZ km^{-1})	−2.85	−2.89	−3.43	−1.88	−6.9	−0.6
Median Z_{DR} at freezing level (dB)	0.12	0.18	0.0	0.44	−0.25	0.94

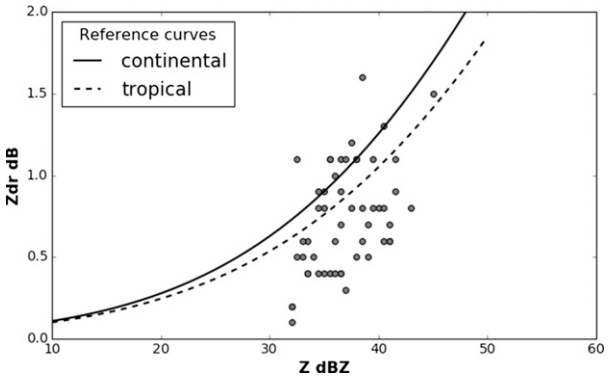

FIG. 5. Median Z and Z_{DR} values in the liquid layer for each warm-rain event plotted in the CZ parameter space; solid and dashed lines represent the Oklahoma and Florida average curves, respectively.

(and thus with different resolution volumes and degrees of beamfilling) in the creation of vertical profiles.

Also notable is that the median slopes of Z_{DR} and K_{DP} in the liquid layer are approximately 0, although the mean slopes are slightly negative ($-0.06\,\mathrm{dB\,km^{-1}}$ and $-0.04^{\circ}\,\mathrm{km^{-2}}$, respectively). The near-zero average slopes likely result from the very low median values of the polarimetric variables in the majority of warm-rain cases (Fig. 4). Despite the near-zero overall slopes of Z_{DR}, an examination of the KR parameter space reveals that the vast majority (42) of cases are associated with positive (median) δZ_{DR} values (Fig. 7). Figure 7 also indicates that the vast majority of the cases (41) are located in quadrant I of the KR parameter space, corresponding to coalescence being the dominant warm microphysical process. It is also notable that only one warm-rain case lies in quadrant II (evaporation dominant) of the KR parameter space, highlighting the moist low-level environments typically associated with warm-rain precipitation events (Grams et al. 2014).

The vertical polarimetric profiles above the freezing level were also analyzed to discern the relative significance of ice- and mixed-phase processes in warm-rain events. Table 1 also includes descriptive statistics regarding the average polarimetric quantities above the freezing level, and Fig. 8 displays histograms of the difference between median echo–storm-top heights and the environmental freezing level. Because of the considerable variation between cases in freezing-level

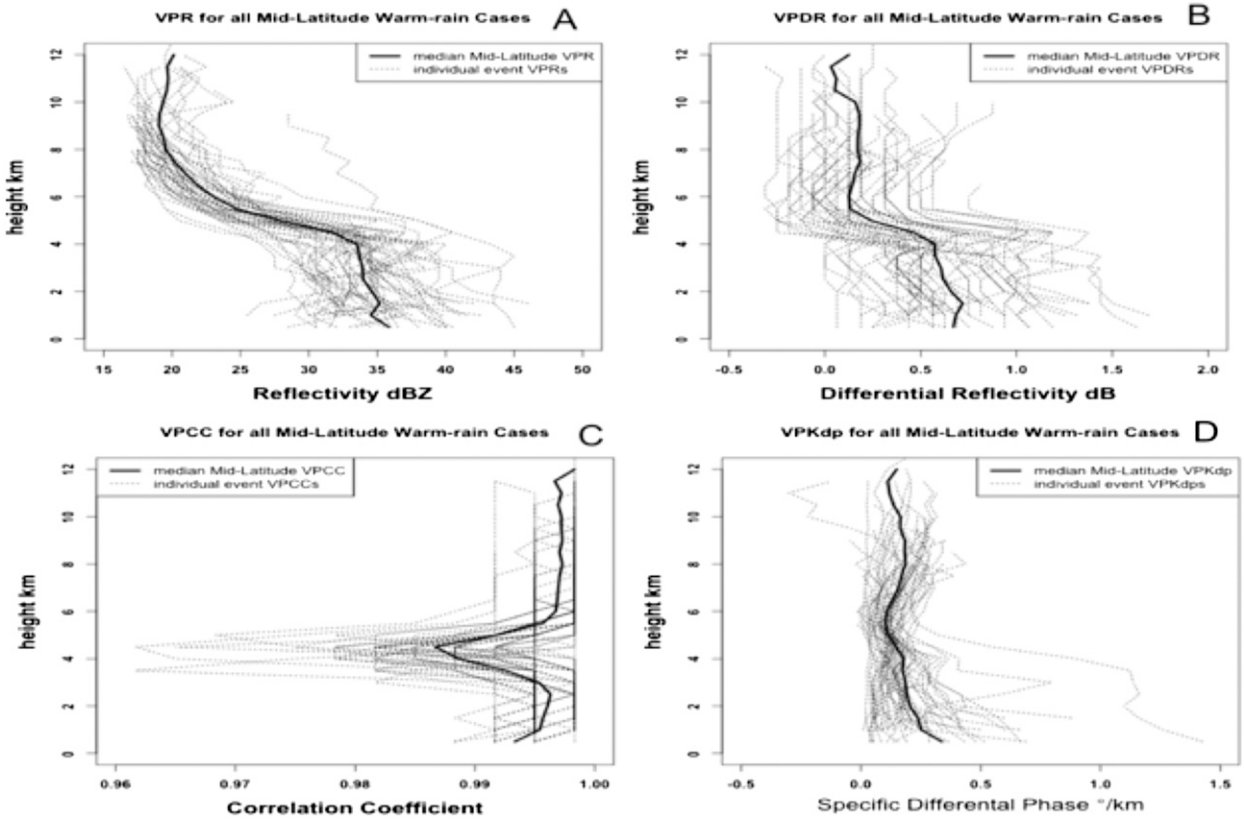

FIG. 6. Vertical profiles of the polarimetric variables (a) Z, (b) Z_{DR}, (c) ρ_{hv}, and (d) K_{DP} for the selected warm-rain events. For each variable, the individual case–median vertical profiles are displayed as dotted lines, while the solid line represents the median profile for all cases aggregated.

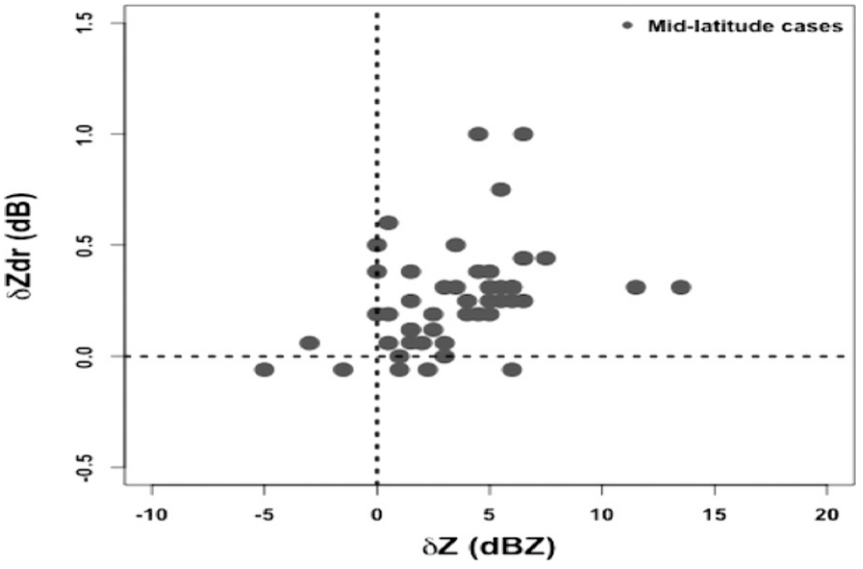

FIG. 7. Median δZ and δZ_{DR} values for each case plotted in the KR parameter space.

height (which ranged from 3.6 to 5 km), the normalized quantity echo-top (storm top) height minus the freezing-level height is analyzed instead of "raw" echo/storm-top heights.

These results demonstrate that in warm-rain events, Z tends to decrease rapidly with height above the freezing level, indicating limited quantities of supercooled water and/or large frozen hydrometeors. Similarly, median Z_{DR} values at the freezing level are quite low (on average around 0.12 dB), also implying limited quantities of supercooled water (the dominant contributor to these variables above the freezing level). However, it should be noted there are four cases with Z_{DR} values at the freezing level >0.5 dB, likely indicating the presence of significant quantities of supercooled water and at least moderately intense updrafts.

Figure 8 shows that, with the exception of two cases, the median echo-top heights (18 dBZ) were located

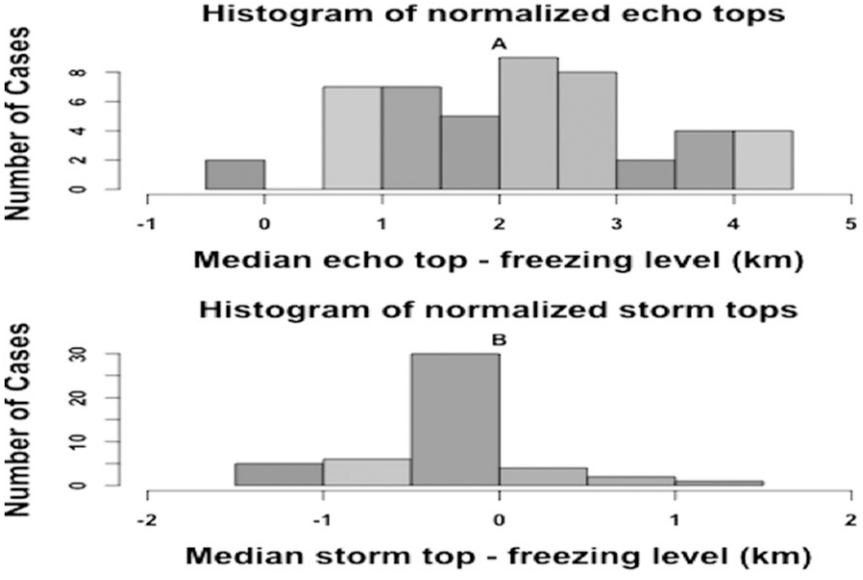

FIG. 8. Histograms of median (a) echo-top (18 dBZ) heights minus freezing-level height and (b) storm-top (30 dBZ) heights minus freezing-level height for the midlatitude warm-rain cases.

above the environmental freezing level; however, storm-top heights (30 dBZ) were located above the freezing level in only 10 out of 49 cases (Fig. 8b). The existence of echo tops above the freezing level points to the presence of at least some hydrometeors (most likely supercooled water or large solid hydrometeors) above the freezing level. However, the limited number of storm tops located above the freezing level implies that these hydrometeors were likely present in limited concentrations and/or were fairly small. Furthermore, there is also evidence of a bright band in many of the vertical profiles (Fig. 6), providing additional evidence of coupling between precipitation growth processes above and below the freezing level, as is generally hypothesized to occur in midlatitude warm-rain precipitation events (Petersen et al. 1999; Vitale and Ryan 2013).

c. *Comparison with non-warm-rain cases*

The previous section documented the polarimetric characteristics associated with midlatitude warm-rain events, and this section compares these characteristics with those observed in non-warm-rain events. This comparison is important in determining the potential utility of a polarimetric warm-rain classification algorithm. The non-warm-rain events analyzed in this section are further divided into non-warm-rain stratiform (NWRS) and non-warm-rain convective (NWRC) events solely on the basis of their MRMS SPT classification. Figure 9a displays the warm-rain and non-warm-rain case medians plotted in the CZ parameter space, and Table 2 shows the median percentages of pixels lying below the two reference curves. It is clear from Fig. 9a and Table 2 that the majority of warm-rain case medians are located below both reference curves (corresponding to higher concentrations of smaller drops), while the majority of NWRC events tend to lie above both curves. Furthermore, a few of the NWRC convective events lying below both curves have median Z values of around 50 dBZ, likely implying hail contamination (which, depending on the size and density of the hail, could also result in depressed Z_{DR} values). Future studies will likely utilize a more conservative hail cap (60 dBZ was employed in this study) to better mitigate this phenomenon. Although the NWRS events also tend to lie above the reference curves, separation between NWRS and warm-rain events on the basis of CZ parameter space is somewhat more tenuous.

Figure 9b displays the locations of the selected cases in the KR parameter space, and from this figure, it is obvious that the vertical variation of Z and Z_{DR} in NWRS events is quite distinct from that observed in NWRC and warm-rain events. Specifically, all NWRS events lie in quadrants II (evaporation dominant) and III (breakup dominant), while most of the warm-rain events lie in quadrants I (coalescence dominant) and IV (coalescence–breakup balance). This result is not unexpected given that precipitation growth in stratiform events is believed to occur primarily above the freezing level, initially via vapor deposition and then via aggregation nearer to the freezing level (Houze 1997). Consequently, since the primary stratiform precipitation growth processes occur above the freezing level, below the freezing level, the dominant microphysical processes are not growth processes at all but rather size-reduction processes such as evaporation or breakup.

An interesting observation from Fig. 9b is that most (25 of 27) NWRC events lie in quadrant I of the KR parameter space. Although a similar result was observed in Kumjian and Prat (2014), the precipitation events analyzed in that study occurred over the tropical Indian Ocean, and the authors anticipated that the dominant warm microphysical process in midlatitude continental convective events would be breakup caused by the larger initial droplets formed from the melting of large hail and graupel. One hypothesis to explain the apparent significance of the coalescence process in NWRC events is that the large raindrops resulting from the melting of hail and graupel act as large collector drops and help initiate the coalescence process. This would represent a coupling between precipitation growth processes above and below the freezing level. Another explanation is that the melting of hail and graupel within the primarily liquid layer produces similar polarimetric signatures as coalescence.

Some support is lent to this second hypothesis, via inspection of the median vertical profiles of Z and Z_{DR} in NWRC precipitation (Fig. 10). It appears that initially the melting of graupel and hail may contribute to enhanced Z and Z_{DR} within the liquid layer because of changes in the dielectric constant and aspect ratio; however, nearer to the surface, when this process is mostly completed, Z and Z_{DR} begin to decrease, signaling that perhaps droplet breakup (or the further decrease in size of melting hailstones caused by shedding) is the dominant microphysical process (Ryzhkov et al. 2013; Ortega et al. 2016). This nonmonotonic vertical variation of Z and Z_{DR} within the liquid layer limits the utility of the KR parameter space, which relies upon simple differences of Z–Z_{DR} between two layers. Furthermore, unlike in primarily stratiform precipitation, where the melting layer is generally narrow (usually on the order of about 500 m) and well defined, in convective precipitation events, the melting layer is much more ambiguous and broad. This likely implies that our assumption that all hydrometeors below our estimated

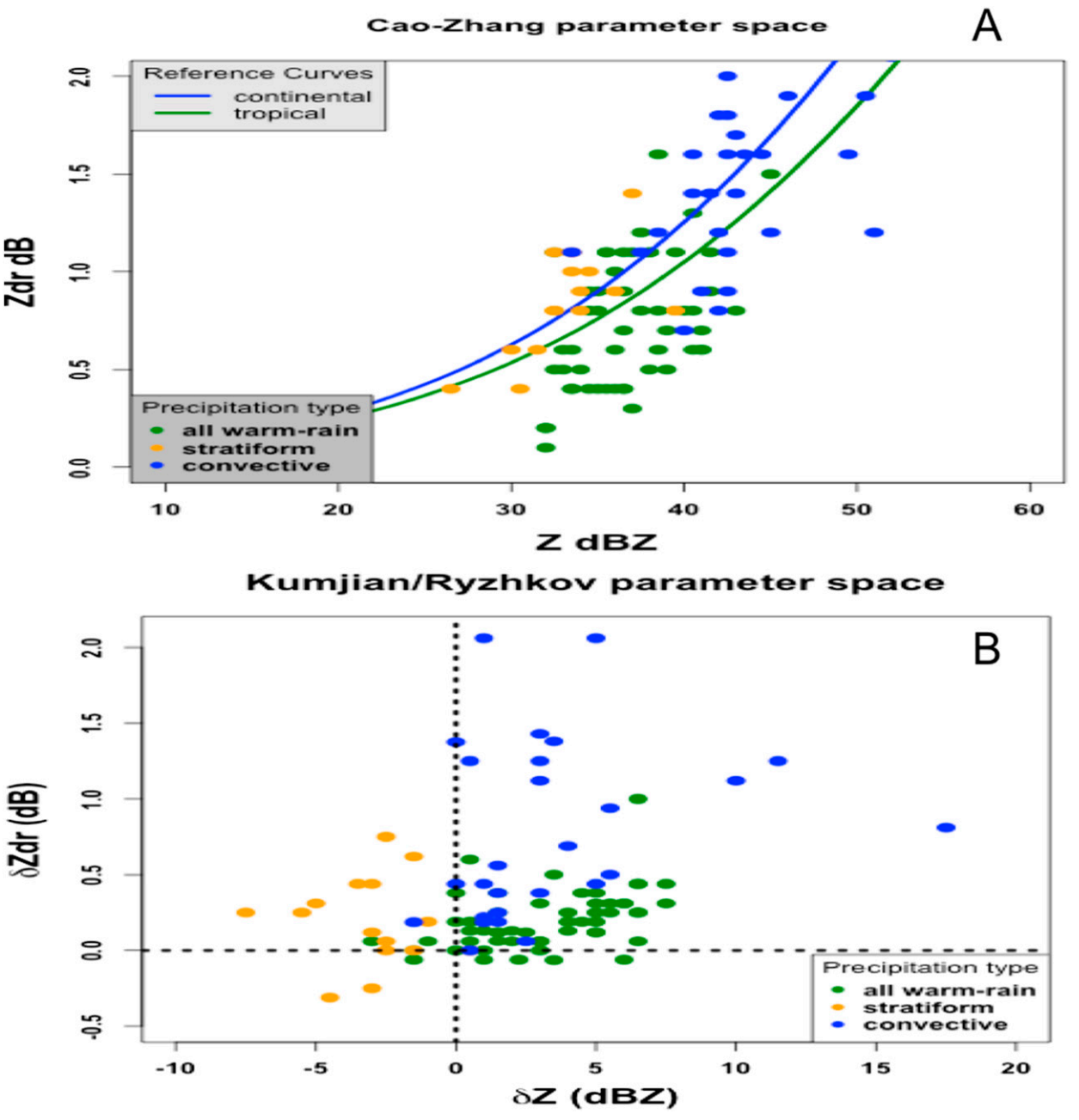

FIG. 9. (a) Median Z and Z_{DR} values in the liquid layer for all non-warm-rain events plotted in the CZ parameter space and colored using the MRMS SPT classification. The blue and green curves represent the Oklahoma and Florida average curves, respectively. (b) As in (a), but for the KR parameter space.

melting-layer bottom are purely liquid does not hold in precipitation events characterized by large rimed hydrometeors.

Table 2 highlights some additional differences between warm-rain and non-warm-rain events. Not surprisingly, NWRC events are typically associated with the highest median values of all the polarimetric variables. Furthermore, NWRC events are associated with higher storm tops relative to the freezing level (in both warm-rain and NWRS events, the storm tops tend to be located below the freezing level, while the storm tops tend to be over 2 km higher than the freezing level in NWRC events) and a slower decrease in reflectivity with height above the freezing level. NWRS events have generally similar liquid-layer polarimetric characteristics as non-warm-rain events; however, notably in NWRS events,

TABLE 2. Medians of selected polarimetric parameters for warm-rain, NWRC, and NWRS events.

	Warm rain	NWRC	NWRS
Median liquid Z (dBZ)	36.75	42.5	33.5
Median liquid Z_{DR} (dB)	0.8	1.4	0.85
Median liquid K_{DP} (° km^{-1})	0.2	0.5	0.2
Pixels below the CZ Oklahoma curve: median (%)	76	47	54
Pixels below the CZ Florida curve: median (%)	66	38	43
Median slope Z liquid phase (dBZ km^{-1})	−0.6	−0.15	0.95
Median slope Z ice phase (dBZ km^{-1})	−2.85	−1.45	−2.7
Median Z_{DR} at freezing level (dB)	0.12	0.15	0.09
Median storm-top height–freezing level (km)	−0.3	2.2	−0.33

reflectivity decreases toward the surface below the melting layer (i.e., the slope of Z is positive in the liquid layer), implying that evaporation and/or breakup are the dominant warm microphysical processes.

4. Conclusions and future research directions

The primary aim of this study was to document the three-dimensional polarimetric characteristics associated with midlatitude precipitation events in order to lay the groundwork for the development of a polarimetric and therefore microphysically based warm-rain classification algorithm. The results of this classification scheme could then be utilized to improve radar QPE. To accomplish this goal, the polarimetric characteristics of 49 carefully selected warm-rain precipitation events and 42 non-warm-rain events were analyzed using Level II NEXRAD data and MRMS data. The analysis focused on precipitation events occurring over the CONUS east of 102°W during the 2014 warm season (April–September). Utilizing radar, rain gauges, and environmental data, warm-rain and non-warm-rain precipitation events were identified and partitioned. Significant results from the polarimetric analysis of the warm-rain events are outlined below:

1) Considerable diversity was observed in the polarimetric characteristics associated with the warm-rain events, which is not unexpected given the large spatiotemporal diversity of the dataset (Fig. 2). However, the majority of warm-rain cases were characterized by median liquid-layer Z values ~(35–40) dBZ, Z_{DR} values ~(0.5–1) dB, and median K_{DP} values of approximately 0.1°–0.5° km^{-1}, implying the presence of relatively small drops. Furthermore, when the cases are mapped in the CZ parameter space, it is

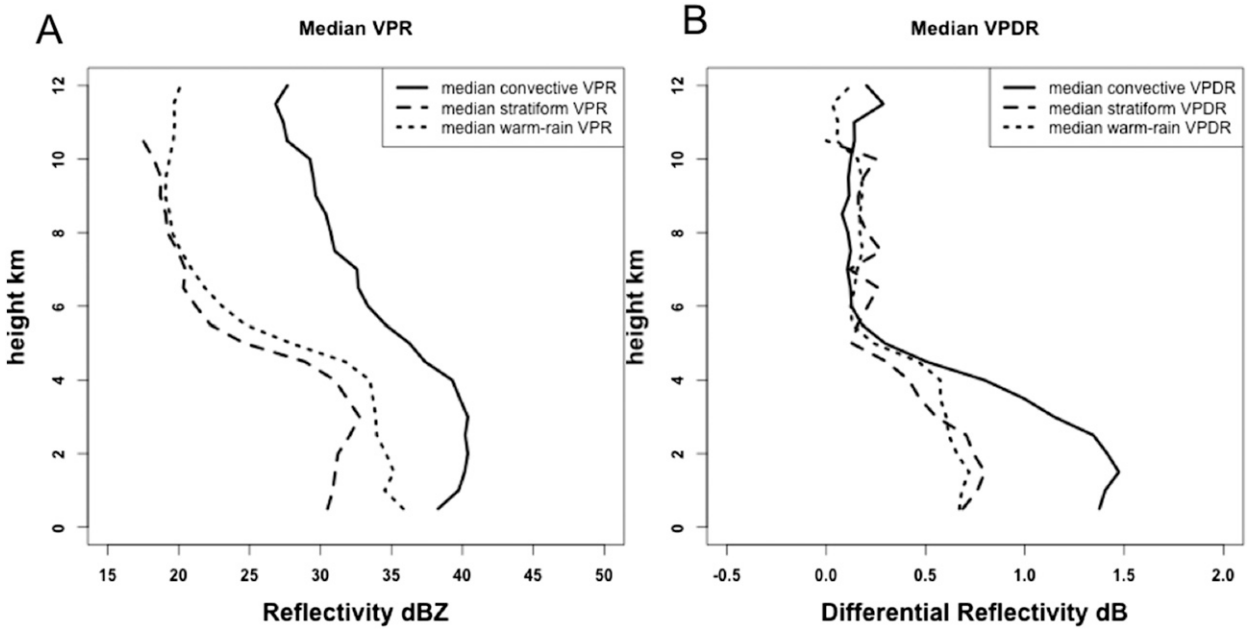

FIG. 10. Median vertical profiles of (a) Z and (b) Z_{DR} for each of the three primary precipitation classification categories.

evident that the majority of cases were characterized by higher concentrations of smaller drops than would be expected for midlatitude precipitation.

2) Regarding the vertical profiles of the polarimetric variables, the majority of cases were associated with negative VPR slopes below the freezing level. The vertical slopes of Z_{DR} and K_{DP} below the freezing level were approximately zero. This result was somewhat surprising, as it was expected that both Z_{DR} and K_{DP} would increase toward the surface in precipitation characterized by enhanced precipitation growth via collision–coalescence. Despite the near-zero slopes of the polarimetric variables, the vast majority of cases were characterized by coalescence being the dominant warm microphysical process as determined using the KR parameter space (Fig. 7).
3) The magnitude and relative significance of precipitation growth processes above the freezing level also varied significantly between warm-rain cases. Almost all warm-rain cases displayed at least some evidence of ice- and mixed-phase precipitation growth processes, as evidenced by median echo tops above the freezing level, median Z_{DR} values >0 at the freezing level, and indications of a melting layer in the median polarimetric profiles. However, the majority of cases were characterized by a $<-3\,\mathrm{dBZ\,km^{-1}}$ decrease in Z with height above the freezing level, low freezing-level Z_{DR} values near 0.1 dB, echo tops 1–3 km above the freezing level (Fig. 8), and storm tops below the freezing level. These results imply limited quantities and sizes of ice-phase hydrometeors and supercooled water and likely indicate relatively limited precipitation growth processes above the freezing level.

The final component of the study compared the polarimetric characteristics associated with the warm-rain events with those observed in 42 non-warm-rain stratiform and convective cases. Based on this comparison, it does appear possible to distinguish warm-rain events and non-warm-rain events using polarimetric data. Specifically, non-warm-rain convective events and warm-rain events can be largely separated using the CZ parameter space, and non-warm-rain stratiform events and warm-rain events can be separated using the KR parameter space. These results imply that the average liquid-layer microphysical characteristics (i.e., high concentrations of small drops) associated with warm-rain events are distinct from those observed in non-warm-rain convective events (low concentrations of large drops), while the dominant warm microphysical processes (i.e., collision–coalescence) associated with warm-rain events are distinct from those observed in non-warm-rain stratiform events (evaporation and breakup).

Although the current state-of-the-science warm-rain identification algorithm (MRMS' SPT algorithm) incorporates information regarding the slope of the VPR to identify warm-rain precipitation (and therefore is somewhat microphysically based), it has been demonstrated that this type of VPR is not unique to warm-rain precipitation and specifically is occasionally present in non-warm-rain convective (particularly when convection is decaying) precipitation events. A polarimetric algorithm, which can better identify the DSDs associated with non-warm-rain convective precipitation, would thus be particularly useful in limiting classification false alarms, which often result in significant QPE overestimation.

This study is only the first step in the development of a polarimetric warm-rain identification algorithm as we are not aware of any comprehensive study documenting and quantifying the three-dimensional polarimetric characteristics associated with midlatitude warm-rain events. The next step in the development of a warm-rain classification algorithm will involve performing the above analysis for another warm season to significantly increase the number of warm- and non-warm-rain cases. This larger sample size can then guide the optimal statistical classification method (e.g., neural network, random forest, fuzzy-logic, and Bayesian multidimensional regression) and also which radar and/or environmental parameters should be incorporated in the chosen model. Additionally, because of the noise inherent in the polarimetric variables, steps would have to be taken to translate the results of this study (which focused on precipitation features that spanned tens of kilometers) to an algorithm that could operate on smaller scales (the current MRMS pixel size is $1\,\mathrm{km^2}$). The specifics of these steps are beyond the scope of this preliminary study, and algorithm development should not be performed until more data are analyzed and the analysis procedure is refined. The final step in the classification scheme would be determining how to evaluate its accuracy. This task is particularly challenging in this context because no strict validation dataset exists. However, it may be possible to utilize ancillary data such as lightning and satellite data in conjunction with radar–gauge QPE comparisons to evaluate the results of the classification algorithm.

Acknowledgments. The authors thank the MRMS development team for access to the MRMS products. This research was supported by the National Aeronautics and Space Administration under Grant NNX13AF84G.

REFERENCES

Adhikari, P., Y. Hong, K. R. Douglas, D. B. Kirschbaum, J. Gourley, R. Adler, and G. R. Brakenridge, 2010: A digitized global flood inventory (1998–2008): Compilation and preliminary results. *Nat. Hazards*, **55**, 405–422, doi:10.1007/s11069-010-9537-2.

Baeck, M. L., and J. A. Smith, 1998: Rainfall estimation by the WSR-88D for heavy rainfall events. *Wea. Forecasting*, **13**, 416–436, doi:10.1175/1520-0434(1998)013<0416:REBTWF>2.0.CO;2.

Cao, Q., G. Zhang, E. Brandes, T. Schuur, A. Ryzhkov, and K. Ikeda, 2008: Analysis of video disdrometer and polarimetric radar data to characterize rain microphysics in Oklahoma. *J. Appl. Meteor. Climatol.*, **47**, 2238–2255, doi:10.1175/2008JAMC1732.1.

Chen, R., Z. Li, R. J. Kuligowski, R. Ferraro, and F. Weng, 2011: A study of warm rain detection using A-Train satellite data. *Geophys. Res. Lett.*, **38**, L04804, doi:10.1029/2010GL046217.

Chen, S., and Coauthors, 2013: Evaluation and uncertainty estimation of NOAA/NSSL next-generation National Mosaic quantitative precipitation estimation product (Q2) over the continental United States. *J. Hydrometeor.*, **14**, 1308–1322, doi:10.1175/JHM-D-12-0150.1.

Giangrande, S. E., J. M. Krause, and A. V. Ryzhkov, 2008: Automatic designation of the melting layer with a polarimetric prototype of the WSR-88D radar. *J. Appl. Meteor. Climatol.*, **47**, 1354–1364, doi:10.1175/2007JAMC1634.1.

Gochis, D., and Coauthors, 2015: The Great Colorado Flood of September 2013. *Bull. Amer. Meteor. Soc.*, **96**, 1461–1487, doi:10.1175/BAMS-D-13-00241.1.

Grams, H. M., J. Zhang, and K. L. Elmore, 2014: Automated identification of enhanced rainfall rates using the near-storm environment for radar precipitation estimates. *J. Hydrometeor.*, **15**, 1238–1254, doi:10.1175/JHM-D-13-042.1.

Houze, R. A., Jr., 1997: Stratiform precipitation in regions of convection: A meteorological paradox? *Bull. Amer. Meteor. Soc.*, **78**, 2179–2196, doi:10.1175/1520-0477(1997)078<2179:SPIROC>2.0.CO;2.

Kirstetter, P.-E., J. J. Gourley, Y. Hong, J. Zhang, S. Moazamigoodarzi, C. Langston, and A. Arthur, 2015: Probabilistic precipitation rate estimates with ground-based radar networks. *Water Resour. Res.*, **51**, 1422–1442, doi:10.1002/2014WR015672.

Kumjian, M. R., and O. P. Prat, 2014: The impact of raindrop collisional processes on the polarimetric radar variables. *J. Atmos. Sci.*, **71**, 3052–3067, doi:10.1175/JAS-D-13-0357.1.

——, A. V. Ryzhkov, S. Trömel, M. Diederich, K. Mühlbauer, and C. Simmer, 2012: Retrievals of warm-rain microphysics using X-band polarimetric radar data. *26th Conf. on Hydrology*, New Orleans, LA, Amer. Meteor. Soc., 406. [Available online at https://ams.confex.com/ams/92Annual/webprogram/Paper206846.html.]

Lakshmanan, V., A. Fritz, T. Smith, K. Hondl, and G. Stumpf, 2007: An automated technique to quality control radar reflectivity data. *J. Appl. Meteor. Climatol.*, **46**, 288–305, doi:10.1175/JAM2460.1.

Lang, T. J., S. A. Rutledge, and R. Cifelli, 2010: Polarimetric radar observations of convection in northwestern Mexico during the North American Monsoon Experiment. *J. Hydrometeor.*, **11**, 1345–1357, doi:10.1175/2010JHM1247.1.

Liu, C., and E. J. Zipser, 2009: "Warm rain" in the tropics: Seasonal and regional distributions based on 9 yr of TRMM data. *J. Climate*, **22**, 767–779, doi:10.1175/2008JCLI2641.1.

Nicosia, D. J., and Coauthors, 1999: A flash flood from a lake-enhanced rainband. *Wea. Forecasting*, **14**, 271–288, doi:10.1175/1520-0434(1999)014<0271:AFFFAL>2.0.CO;2.

Ortega, K. L., J. M. Krause, and A. V. Ryzhkov, 2016: Polarimetric radar characteristics of melting hail. Part III: Validation of the algorithm for hail size discrimination. *J. Appl. Meteor. Climatol.*, **55**, 829–848, doi:10.1175/JAMC-D-15-0203.1.

Petersen, W. A., and Coauthors, 1999: Mesoscale and radar observations of the Fort Collins flash flood of 28 July 1997. *Bull. Amer. Meteor. Soc.*, **80**, 191–216, doi:10.1175/1520-0477(1999)080<0191:MAROOT>2.0.CO;2.

Qi, Y., J. Zhang, and P. Zhang, 2013: A real-time automated convective and stratiform precipitation segregation algorithm in native radar coordinates. *Quart. J. Roy. Meteor. Soc.*, **139**, 2233–2240, doi:10.1002/qj.2095.

Rutledge, S. A., D. Wolff, B. Dolan, P. Kennedy, W. Petersen, and V. Chandrasekar, 2013: Microphysical variability of tropical and mid-latitude rainfall as revealed by polarimetric radar. *2013 Fall Meeting*, San Francisco, CA, Amer. Geophys. Union, Abstract H42A-02.

Ryzhkov, A. V., S. E. Giangrande, and T. J. Schuur, 2005: Rainfall estimation with a polarimetric prototype of WSR-88D. *J. Appl. Meteor.*, **44**, 502–515, doi:10.1175/JAM2213.1.

——, M. R. Kumjian, M. S. Ganson, and A. P. Khain, 2013: Polarimetric radar characteristics of melting hail. Part I: Theoretical simulations using spectral microphysical modeling. *J. Appl. Meteor. Climatol.*, **52**, 2849–2870, doi:10.1175/JAMC-D-13-073.1.

Squires, P., 1956: The micro-structure of cumuli in maritime and continental air. *Tellus*, **8**, 443–444, doi:10.3402/tellusa.v8i4.9040.

Ulbrich, C. W., and D. Atlas, 2008: Radar measurement of rainfall with and without polarimetry. *J. Appl. Meteor. Climatol.*, **47**, 1929–1939, doi:10.1175/2007JAMC1804.1.

Vasiloff, S. V., and Coauthors, 2007: Improving QPE and very short term QPF: An initiative for a community-wide integrated approach. *Bull. Amer. Meteor. Soc.*, **88**, 1899–1911, doi:10.1175/BAMS-88-12-1899.

Vitale, J. D., and T. Ryan, 2013: Operational recognition of high precipitation efficiency and low-echo-centroid convection. *J. Oper. Meteor.*, **1**, 128–143, doi:10.15191/nwajom.2013.0112.

Xu, X., K. Howard, and J. Zhang, 2008: An automated radar technique for the identification of tropical precipitation. *J. Hydrometeor.*, **9**, 885–902, doi:10.1175/2007JHM954.1.

Zhang, G., J. Sun, and E. A. Brandes, 2006: Improving parameterization of rain microphysics with disdrometer and radar observations. *J. Atmos. Sci.*, **63**, 1273–1290, doi:10.1175/JAS3680.1.

Zhang, J., K. Howard, and J. J. Gourley, 2005: Constructing three-dimensional multiple-radar reflectivity mosaics: Examples of convective storms and stratiform rain echoes. *J. Atmos. Oceanic Technol.*, **22**, 30–42, doi:10.1175/JTECH-1689.1.

——, and Coauthors, 2011: National Mosaic and Multi-Sensor QPE (NMQ) system: Description, results, and future plans. *Bull. Amer. Meteor. Soc.*, **92**, 1321–1338, doi:10.1175/2011BAMS-D-11-00047.1.

——, and Coauthors, 2016: Multi-Radar Multi-Sensor (MRMS) quantitative precipitation estimation: Initial operating capabilities. *Bull. Amer. Meteor. Soc.*, **97**, 621–638, doi:10.1175/BAMS-D-14-00174.1.

Zipser, E. J., and K. R. Lutz, 1994: The vertical profile of radar reflectivity of convective cells: A strong indicator of storm intensity and lightning probability? *Mon. Wea. Rev.*, **122**, 1751–1759, doi:10.1175/1520-0493(1994)122<1751:TVPORR>2.0.CO;2.

Zrnic, D. S., and A. V. Ryzhkov, 1999: Polarimetry for weather surveillance radars. *Bull. Amer. Meteor. Soc.*, **80**, 389–406, doi:10.1175/1520-0477(1999)080<0389:PFWSR>2.0.CO;2.